Proceedings of IMECE'03
2003 ASME International Mechanical Engineering Congress
Washington, D.C., November 15–21, 2003

IMECE2003-42659

DESIGN OF A CONFORMABLE ROTOR AIRFOIL USING DISTRIBUTED PIEZOELECTRIC ACTUATION

Phuriwat Anusonti-Inthra
Postdoctoral Fellow
Dept. of Aerospace Engineering

Farhan Gandhi
Associate Professor
Dept. of Aerospace Engineering

Mary Frecker
Associate Professor
Dept. of Mechanical and Nuclear Engineering

The Pennsylvania State University
University Park, PA 16802

ABSTRACT

In the present study, a design methodology is developed for determining the optimal distribution of a limited amount of piezoelectric material and optimal skin for a conformable rotor airfoil section. The objective of the design optimization is to generate a conformable airfoil structure that produces significant trailing edge deflection under actuation loads, but minimal airfoil deflection under aerodynamic loads. Energy functions, Mutual Potential Energy (MPE) and Strain Energy (SE), are used as measures of the deflections created by the actuation and aerodynamic loads, respectively. The design objective is achieved by maximizing a multi-criteria objective function that represents a ratio of the MPE to SE. Several design optimization techniques are evaluated including geometry and concurrent geometry-topology optimizations. The results of the study indicate that the optimized conformable airfoil section obtained using the concurrent geometry-topology optimization can produce a significant downward trailing edge deflection, and the airfoil deformation due to the aerodynamic loads alone is small. However, the optimized airfoil design is extremely complex and contains intricate network of actuators, which may be difficult to fabricate. Systematic simplification of the structure is performed to obtain a conformable airfoil design that is simple and may be easy to build. Further parametric optimization is used to find optimal values of the skin axial and bending stiffness for an optimal conformable airfoil design. The airfoil can produce a downward trailing edge deflection equivalent to 3.7° of Effective Flap Angle from the actuation loads, with the peak-to-peak deflection being nearly twice the downward deflection, and the airfoil deformation due to the airload loads is less than 1°. The optimal skin should have less axial stiffness and much more bending stiffness as compared to a conventional skin.

1. INTRODUCTION

The blades of the main rotor of a helicopter are generally long and slender (having a high aspect ratio), and rather flexible along the span, but relatively rigid along the cross-section. The cross-section, shaped like an airfoil to provide lift, is rigid by design, since any change in airfoil profile as a result of the loading on the cross-section could, in turn, significantly affect the aerodynamic lift and the performance of the airfoil. While an uncommanded change in airfoil profile would obviously be undesirable, a deliberate change in airfoil shape could intentionally be induced and exploited, for example, to ensure optimal performance, even as the flight condition varies. In addition to improving performance, a cyclic change in the airfoil profile over every rotor revolution could be used to generate unsteady aerodynamic loads that could cancel the vibratory loads on the rotor blades. In this respect, a continuously deformable, or conformable rotor blade airfoilwould be a successor to rotor blade airfoils with trailing-edge (TE) flaps, which are already being extensively considered for helicopter vibration reduction [1]-[11]. Virtually all of the research efforts focusing on rotor TE flaps for vibration reduction have used piezoelectric ceramic material for the actuators that deflect the flaps, since these actuators are solid-state, compact and can produce a very large force at high frequency. However, the stroke of piezoelectric actuators is

usually very small, so a mechanical amplification of the stroke is necessary. Examples of these actuator-amplifier mechanisms include Double-L piezostack actuators [5], C-block actuators [6]-[7], X-frame actuators [8], and bimorph-lever benders [10]. Continuously conformable rotor airfoils will also be required to use a piezoelectric based actuation system to meet the frequency requirements (other solid state actuation concepts based on "smart" materials such as shape memory alloys do not have the required frequency bandwidth even though they can provide a larger stroke), while design optimization could be exploited to produce the required stroke amplification. The idea of using such a smart-materials based continuously conformable rotor airfoil was first suggested by Ormiston [12].

Continuously deformable airfoils have already been considered to improve performance and handling qualities (low frequency actuation) of fixed wing aircrafts. For example, Kota and Saggere [13] suggested the use of passive compliant structures with a generic force actuator to produce static shape control of an airfoil camber; and Lagoudas and Strelec [14] considered the design of a reconfigurable wing actuated by SMA wires in order to maximize lift-to-drag ratio. A flexible flap system using active deformable rib structures was studied as a part of DLR Adaptive Wing Project, and camber variations of ±15 deg. were achieved using SMA tube [15]. Kudva *et al.* [16], as a part of the Smart Wing program, developed deformable airfoil surfaces using ultrasonic piezoelectric motors and demonstrated that the airfoil could achieve trailing edge deflections of up to 20 deg. Raney *et al.* [17] designed and tested a smooth adaptive wing with a variable thickness skin using SMA actuators. Achievable deflections were 8° and 3° for the trailing edge and leading edge, respectively. Despite the significant deflections, the SMA based actuators may not be suitable for rotor vibration reduction due to their bandwidth limitation.

The design philosophy of the conformable airfoil can be adapted from that of compliant mechanisms, which also achieve desirable motion by undergoing elastic deformation [18]. One approach for designing compliant structures is to apply a topology design optimization method to determine the optimal distribution of available passive and/or active material in a design domain. Ananthasuresh *et al.* [19] has employed topology optimization for the design of compliant MEMS. To maximize the geometric advantage or to maximize the mechanical efficiency, Frecker *et al.* developed a multi-criteria topology optimization approach that had been applied for designing compliant hand-held devices [20] and compliant mechanical amplifiers for piezoelectric stack (d_{33}-type) actuators [21]. For multiple materials, a material interpolation scheme was developed for topology optimization of compliant mechanisms [22]. A two-stage optimization process was introduced by Kota *et al.* [23], who proposed a second-stage size and shape optimization procedure that incorporated stress constraints on passive compliant elements. Additionally, several researchers have studied the topology optimization of different actuators, including a two-phase compliant actuator designed to maximize the work performed on an elastic workpiece [24] and flextensional actuators with piezoelectric material, where the topology of the passive material is optimized [25].

2. FOCUS OF THE PRESENT STUDY

The primary focus of the present study is to develop a design methodology for a smart material-based conformable rotor airfoil, specifically using distributed piezoelectric actuation material aft of the spar to generate cyclically controllable camber for helicopter vibration reduction. Design optimization methodologies using topology and geometry optimizations for calculating the optimal distribution of active material within the airfoil section are developed and implemented. A key consideration in the design is that the optimized airfoil section should be flexible and produce significant trailing edge deflection under actuation load, while being simultaneously stiff and maintaining its shape under aerodynamic loading. Systematic simplification using the optimal design process is performed to achieve a design that meets all the requirements and is relatively simple to construct. Optimal airfoil skin properties are determined using another parametric optimization.

3. ANALYTICAL MODEL

In the present study the rotor blade is assumed to have a NACA-0012 airfoil section [26], an aluminum skin of 1 mm thickness, and a chord length of 1.66 ft. A very rigid D-spar, the primary load carrying member, extends from the leading edge of the airfoil to quarter chord (Fig. 1a). The rigid D-spar is assumed not to undergo any deformation, and consequently, the section aft of the D-spar is clamped at quarter chord, as presented in Fig. 1b.

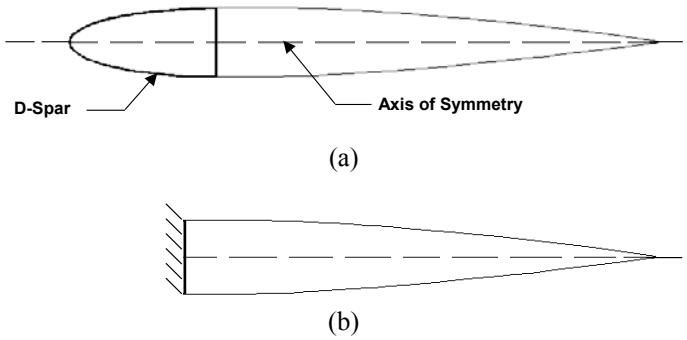

Figure 1: Schematics of (a) an NACA-0012 airfoil section, (b) airfoil section with very rigid D-spar

To actuate the airfoil section at high frequency (in the range of 20 Hz for full scale applications and higher frequency

for scaled rotors) the active elements are chosen to be of piezoelectric ceramic material because of its fast response time. Stack actuator configuration, utilizing the d_{33} effect, is chosen for its high force output. The active elements are distributed *symmetrically about the centerline* within the structure (as shown in Fig. 2), since both upward as well as downward deflections are necessary to generate the required unsteady aerodynamic loads to reduce vibration. The internal structure is modeled as a network of active elements called a ground structure. Each active element in the ground structure represents an individual stack actuator. Finite element modeling is employed to analyze the structure, with the skin modeled using frame elements that allow both bending and axial deformations, while the actuators are modeled using truss elements that have only axial deformation, with pinned connections between the successive frame-truss or truss-truss elements.

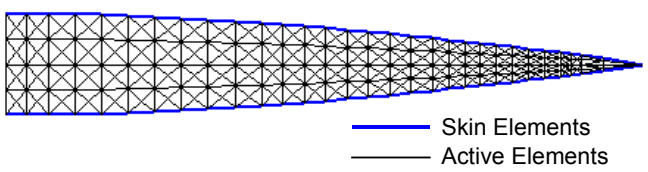

Figure 2: Distribution of active elements within the ground structure

The equivalent axial loading generated by actuation of the i^{th} active element can be expressed as follows:

$$f^{i}_{act} = \frac{E_i A_i d_{33} V_i}{t_c} \qquad (1)$$

where E_i, A_i, d_{33}, t_c, and V_i are actuator modulus of elasticity, cross sectional area, piezoelectric strain constant, thickness of the piezoelectric layers, and applied voltage, respectively. Equal and opposite voltages are applied to actuators located in the top and bottom sections of the structure to effectively generate bending loads on the structure. The displacement field induced by the active elements, u, is calculated using Eq. (2),

$$Ku = F_{act} \qquad (2)$$

where K is the global stiffness matrix and F_{act} is the global load vector due to actuation loads obtained by assembly of the elemental load vectors.

Aerodynamic loading of the airfoil section is calculated numerically using a linear-strength vortex panel method [27]. Fig. 3 shows the variation of pressure coefficient, Cp, on the airfoil surfaces for the NACA 0012 airfoil at 5° angle of attack. The resulting aerodynamic pressure, p, at any point on the surface can then be calculated from this pressure coefficient using Eq. (3),

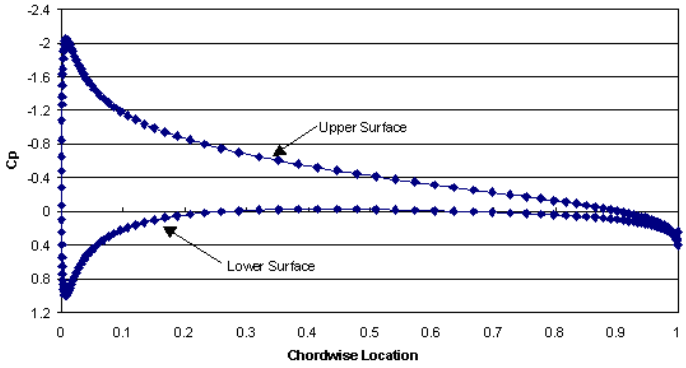

Figure 3: Aerodynamic pressure of the NACA-0012 at a 5° angle of attack

$$p = \frac{1}{2}\rho V_{\infty}^{2} Cp \qquad (3)$$

where ρ is air density and V_{∞} is free-stream velocity. Using this surface pressure, the aerodynamic forces acting on a skin element can be determined by multiplying the surface pressure by the surface area of the skin element. Based on the aerodynamic forces, the aerodynamic loads acting at each node on the skin can be calculated, (the vertical nodal aerodynamic forces are shown graphically in Fig. 4).

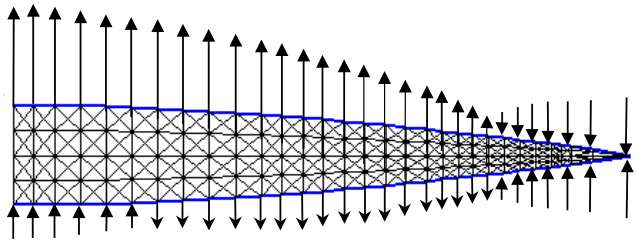

Figure 4: Aerodynamic load distribution on the airfoil structure

The displacement field induced by these aerodynamic forces, w, is expressed in Eq. (4),

$$Kw = F_{aero} \qquad (4)$$

where F_{aero} is the global load vector due to the aerodynamic forces after assembling the elemental aerodynamic load vectors. Although the aerodynamic loading would undergo variation as the airfoil deforms under the actuation loading, these variations are not considered in calculating F_{aero} in Eq. 4. This can be justified in the following terms: The reason for calculating the displacement in Eq. 4 is to ensure that as the material distribution within the airfoil section aft of the spar is varied during the design optimization process, the airfoil does not become overly flexible under aerodynamic loading. In this regard, the baseline aerodynamic surface pressure distribution is adequate and considering the perturbations in pressure

distribution due to variation in camber are not expected to a provide different conclusion.

4. OPTIMIZATION PROBLEM

4.1 Objective Function

The problem of achieving shape change is modeled as one of maximizing the vertical deflection at the trailing edge. The structure with maximum trailing edge deflection, however, may be too flexible to withstand the aerodynamic loads, so a multi-criteria optimization problem is considered. The objective of the optimization problem is to simultaneously - *(i)* maximize the vertical deflection at the *trailing edge* of the airfoil section due to actuation load, and *(ii)* minimize the deflection of the *entire* airfoil section due to aerodynamic load.

The first objective can be achieved by maximizing an energy function, Mutual Potential Energy (*MPE*), of the structure [28]. The *MPE* is defined as follows;

$$MPE = v^T K u \tag{5}$$

where v is a reference displacement field created by a dummy load, which will be described later in this section, and u is the displacement field induced by the actuators (Eq. 2). Thus the first objective function can be written as,

$$max(J_1 = MPE) \tag{6}.$$

To model the deflection at the trailing edge, the unit dummy load method is used. A unit load is applied at the point of interest in the desired direction, i.e. at the trailing edge in the downward direction (Fig. 5), and a virtual displacement field v is calculated using Equation 7,

$$Kv = F_{dummy} \tag{7}$$

where F_{dummy} is the global load vector due to the dummy load. A unit dummy load is applied in the downward vertical direction in order to deflect the trailing edge downward. Due to the symmetry of the design, upward deflection of the trailing edge can be obtained by simply reversing the polarity of the actuation voltage.

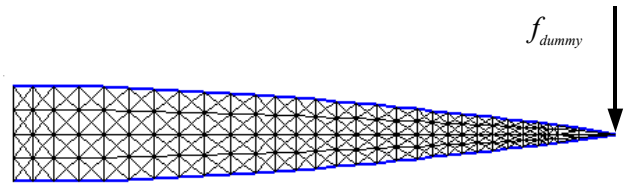

Figure 5: A unit dummy load on the structure

For the second objective, another energy function, Strain Energy (*SE*), is introduced as a measure of the deflection due to the aerodynamic loads. The *SE* is defined as follows:

$$SE = w^T K w \tag{8}$$

where w is described in Eq. 4. To facilitate the inclusion of this objective into one multi-criteria objective function, it is desirable to modify this minimization of the *SE* to a maximization problem. The modified objective function can be expressed as:

$$max\left(J_2 = \frac{1}{SE}\right) \tag{9}$$

The two objective functions are combined to form one multi-criteria objective function using a ratio approach first proposed in Ref. [20] for passive compliant mechanisms. The objective function is defined as:

$$J = max\left(\frac{MPE}{SE}\right) \tag{10}$$

This type of objective function has some advantages and disadvantages over other conventional multi-criteria objective functions (e.g. weighted sum types). One advantage is that the solution does not depend on the selection of the scalar weighting factors or on the order of magnitude of the two objective functions. However, the ratio function requires the use of a non-linear optimization process.

4.2 Optimization Variables

Both the topology and the geometry of the ground structure shown in Figure 2 are to be optimized. Topology optimization can be thought of as determining the optimal connectivity of active structural elements within the airfoil cross-section. Geometry optimization consists of adjusting the location of the connection points between elements, while leaving the topology unchanged. In topology optimization, the cross-sectional areas of the active elements, A_i, are adjusted to maximize the objective function. This topology optimization will effectively increase the cross-sectional area of actuators that are highly effective and reduce the size of actuators that are less effective. Each variable, A_i, is bounded between a minimum and a maximum allowable value as follows;

$$0 < A_{min} \le A_i \le A_{max} \tag{11}$$

where A_{min} and A_{max} are the minimum and maximum limits of cross-sectional area of any active element, respectively. A_{min} is set to a very small number so that the elements that reach this lower limit can be ignored, and the remaining elements make up the optimal topology. An example of a topology network is shown in Fig. 6. The cross-sectional area of the skin elements is unchanged during this topology optimization. Another optimization constraint is the total amount of active material, which is represented by active material volume defined as follows for M total active elements;

$$Vol = \sum_{i=1}^{M} l_i A_i \qquad (12)$$

where l_i is the length of the ith stack actuator. The volume constraint is expressed in terms of percentage of the maximum possible active material volume:

$$Vol_{max} = \sum_{i=1}^{M} l_i A_{max} \qquad (13)$$

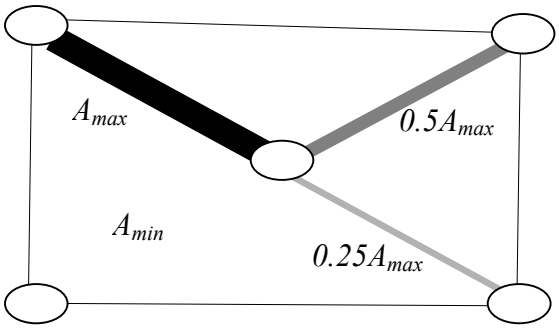

Figure 6: Topology network of active elements, with different sizes

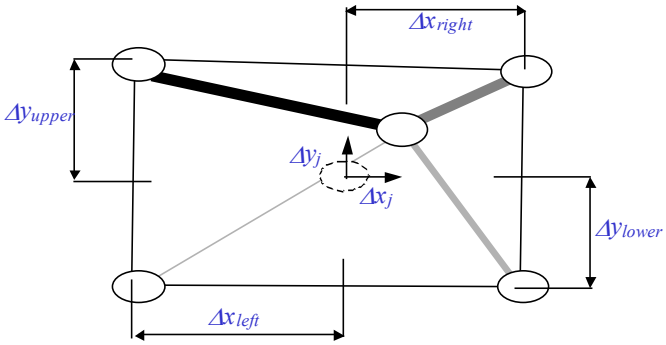

Figure 7: Schematic of geometry modification of actuator network

In geometry optimization, the nodal coordinates (x_j, y_j) of the active element network are modified to maximize the objective function. In essence, this geometry optimization will move nodes connecting the active elements to maximize their effectiveness (defined by the objective function). Modification of one nodal coordinate in an actuator network is shown schematically in Fig. 7. The change in nodal coordinates, Δx_j and Δy_j, is confined within coordinates of the neighboring nodes as described in Eq. 14.

$$\Delta x_{left} \le \Delta x_j \le \Delta x_{right} \qquad (14)$$
$$\Delta y_{lower} \le \Delta y_j \le \Delta y_{upper}$$

It should be noted that it is possible that the nodal coordinates of one node may coincide with those of another node. Nodal coordinates of the skin and the centerline elements are not modified in this geometry optimization.

In both topology and geometry optimizations, the symmetry of the conformable airfoil structure about the axis of symmetry must be maintained. This can be satisfied by imposing the symmetry condition as a constraint in the optimization process. This symmetry constraint could not be imposed in the structural analysis (using only half of the structure for analysis), because the aerodynamic loads are not symmetric.

4.3 Optimization Techniques

In the present study, several optimization techniques are considered. Geometry and concurrent topology-geometry optimizations are considered and are explained in detail next. Detailed description of the topology optimization method can be found in [29].

The geometry optimization problem with a flowchart given in Fig. 8 is solved using the SLP algorithm, which is a gradient-based optimization method (requiring linearization of the objective function and constraints). Gradients of the objective function with respect to the geometry variables are calculated analytically and are presented in the Appendix. The algorithm begins with an initial geometry, and an appropriate change in the geometry is calculated using a small step size. The geometry update process repeats until the objective function is converged.

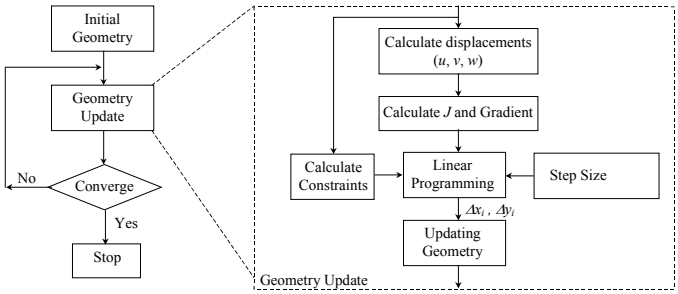

Figure 8: Flowchart of the geometry optimization process using the Sequential Linear Programming algorithm

A Concurrent Geometry-Topology (CGT) optimization is also introduced, and the flowchart of this CGT optimization is given in Fig. 9. The algorithm starts with an initial configuration, and N iterations of topology optimization (see Ref. 29 and a summarized flowchart in Fig. 10) are performed on this initial configuration. Then the topology-optimized structure is used as an initial structure for another M iterations of the geometry optimization. The geometry-optimized structure is sent back to the topology optimization, and the whole process repeats until a convergence criterion is met.

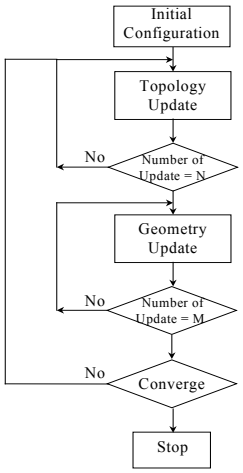

Figure 9: Flowcharts of concurrent geometry-topology optimizations

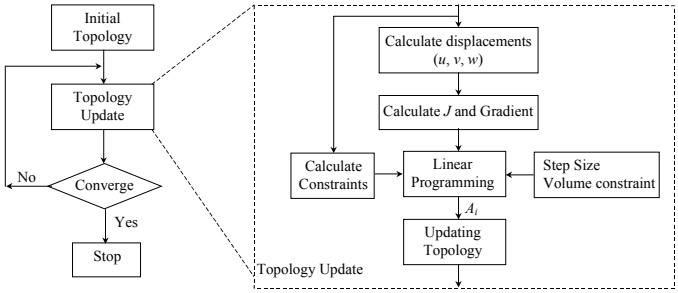

Figure 10: Flowchart of the topology optimization process using the Sequential Linear Programming algorithm

5. RESULTS AND DISCUSSION

5.1 Baseline Configuration

The ground structure is shown in Fig. 2, which is made up of a network of truss and frame elements, with properties presented in Table 1. The structure has 656 active truss elements representing piezoelectric ceramic stack actuators and 62 aluminum passive frame elements to model the skin. The airfoil deflection will be measured using an Equivalent Flap Angle (*EFA*), which is defined as follows;

$$EFA = tan^{-1}\left(\frac{u_{tip}}{0.15c}\right) \qquad (15)$$

The *EFA* produces the same tip deflection as a flapped airfoil with a hinge at 15% chord from the trailing edge.

Table 1: Properties of airfoil structure

Parameter		Value
Piezoelectric Stack Actuators (Truss elements)	Young's Modulus, E	60×10^{9} N/m^2
	Applied Voltage, V_i	+150 V (above sym. axis) −150 V (below sym. axis)
	Piezoelectric constant, d_{33}	640×10^{-12} m/V
	Thickness of piezoelectric layers, t_c	0.00011 m
Airfoil Skin (Frame elements)	Young's Modulus, E	30×10^{9} N/m^2
	Cross sectional area, A	6.35×10^{-6} m^2
	Area moment of inertia, I	5.3×10^{-13} m^3
Aerodynamic properties	Air density, ρ	1.225 kg/m^3
	Airfoil velocity, V_∞	200 m/s

5.2 Topology optimization

Topology optimization is performed following the approach cited in Ref. 29 using the ground structure shown in Figure 2. The initial values of the design variables, the cross sections of the active elements, are randomly generated. Each variable must be bounded within allowable limits (see Eq. 11 and Table 2), and the total active material volume is constrained to 50% of Vol_{max} (defined in Eq. 13). The geometry of the structure is unchanged during the topology optimization.

Table 2: Topology optimization constraints

Constraints	Value
A_{max}	2.6×10^{-5}m^2
A_{min}	1×10^{-9} m^2

The result from the topology optimization is shown in Fig. 11. The optimal topology is shown in grayscale. In this figure the active elements that have reached or are close to A_{min} are not shown, those that have reached A_{max} are shown as black, and the intermediate elements are in shades of gray. For simplicity of interpretation, the airfoil section is divided into four regions – *(i)* a region from 1/4 to 3/8 chord, *(ii)* a region from 3/8 to 1/2 chord, *(iii)* a region from 1/2 to 7/8 chord, and *(iv)* a region from 7/8 chord to the trailing edge (see Fig. 11).

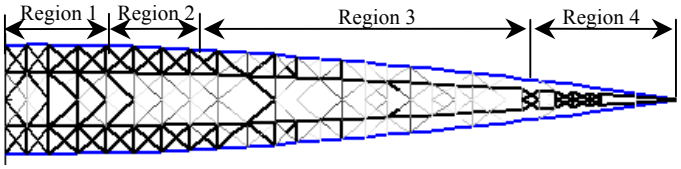

Figure 11: Topology optimization result with a volume constraint of 50% Vol_{max}: (J = 0.12 and EFA = -3.99º)

The result shows that the optimal topology is one in which the active elements form a structure that is generally parallel to the skin in regions 1, 2, and 3; close to the skin in regions 1 and 2; and near axis of symmetry in region 4. The active elements

that are reduced in size to reach A_{min} are in the centerline; in areas close to the centerline in regions 2 and 3; in areas near the skin in regions 3 and 4. This optimal topology with the objective function of 0.12 can produce an *EFA* of 3.99° under the actuation loads and allows *EFA* of 0.54° under the airloads.

5.3 Geometry optimization

Geometry optimization is performed using the optimal topology shown in Fig. 11 as an initial configuration, which can produce an *EFA* of 3.99° and a *J* of 0.12 with volume constraint of 50% of Vol_{max} (defined in Eq.13). The cross-sectional areas of all elements are kept unchanged during the geometry optimization process. The results of the geometry optimization are shown in Fig. 12. The process converges after approximately 180 iterations as shown in Fig. 12a, with objective function increasing from 0.12 to 0.26 (a 117% increase from the initial configuration), and the optimized geometry is shown in Fig. 12b. It is interesting, however, to note that the geometry optimization produces an Effective Flap Angle of 3.42°, which represents a 15% reduction from the original value. The corresponding airfoil deflection due to the aerodynamic loads alone is 0.25° (almost 50% reduction from the 0.54° airload angle of the initial configuration). This suggests that the significant increase in objective function is due primarily to reduction in strain energy. Comparing Fig. 12 to Fig. 11, the result shows little change in geometry of the active elements in regions 3 and 4. The active elements in region 1 are shifted toward the skin. Region 2 is a transitional area where the active elements near region 1 are shifted toward the skin, and the active elements gradually shifting away from the skin to connect with active elements near region 3.

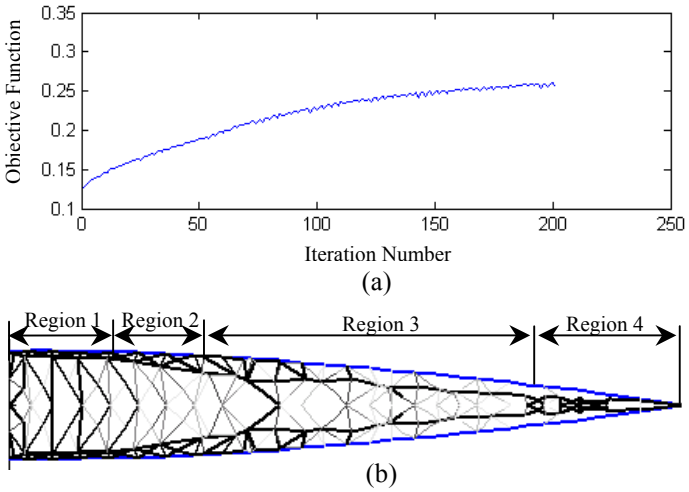

Figure 12: Geometry optimization results with a volume constraint of 50% Vol_{max}: (a) convergence history, J = 0.26, (b) optimized geometry, EFA = -3.42°

5.4 Concurrent Geometry-Topology (CGT) optimization

The concurrent optimization is performed using 21 iterations of topology and geometry optimizations (i.e., N, M equal to 21) and with volume constraint of 50% of Vol_{max}. The initial configuration is the structure shown in Fig. 11, which initially produces an equivalent flap angle of 3.99° and has an objective function of 0.12. The constraints for the topology optimization are given in Table 2. The results from the CGT optimization are presented in Fig. 13. The convergence history (Fig. 13a) shows that the CGT optimization process converges after 630 iterations (15 repetitions of the geometry and topology optimization cycles). The optimized structure, illustrated in Fig. 13b, can produce an *EFA* of 4.3° (a 9% increase from the original configuration), with an objective function of 0.34 (a 183% increase). The airfoil deformation due to the aerodynamic loads is 0.26°. The active elements that are increased in size to reach A_{max} are concentrated in areas close to the skin in regions 1 and 2, and scattered in areas near the centerline in regions 3 and 4. The active elements that are reduced in size to A_{min} are distributed in areas near the centerline in all regions. In comparison, the results obtained using geometry and CGT optimizations are slightly different. The main distinction is that the CGT optimized structure does not have a clear transitional area where the active elements are gradually shifted toward the skin.

With the volume constraint of 50% of Vol_{max}, the optimized structure shown in Fig. 13 is extremely complex and contains more than 100 pairs of actuators of varying sizes. In the following sections, an effort to systematically simplify the structure is presented by re-optimizing the structure with successively tighter volume constraints. The effects of skin parameters on the optimized topology are also provided.

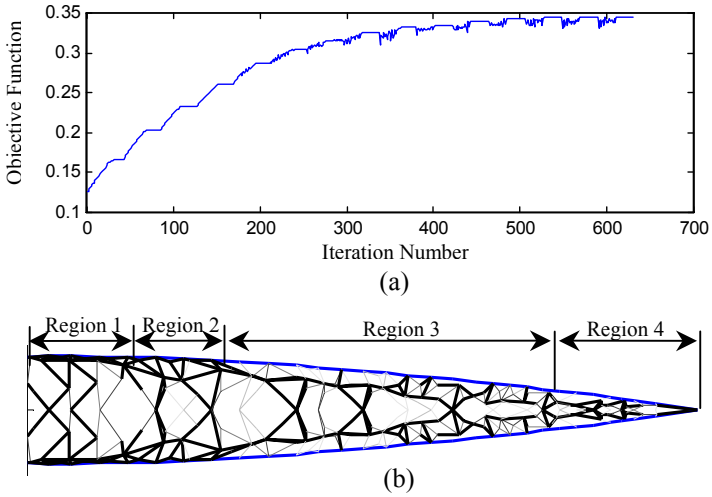

Figure 13: Concurrent Geometry-topology optimization results with a volume constraint of 50% Vol_{max}: (a) convergence history, J = 0.34, (b) optimized structure, EFA = -4.33°

5.4.1 Volume Constraint

The topology solutions, maximum deformations (shown exaggerated by a factor of 7), and corresponding axial strain

level of the CGT optimized structures using volume constraints of 50, 30, 20, 10, and 5% of Vol_{max} are presented in Fig. 14.

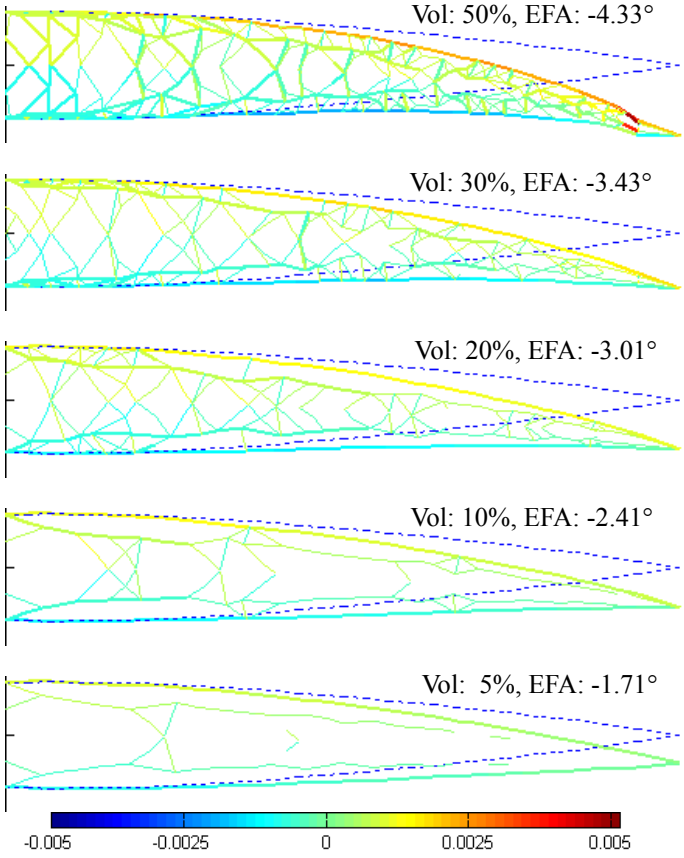

Figure 14: Topologies, deformations (7x), and axial strain level (color coded) of CGT optimized structures for different volume constraints (50, 30, 20,10, and 6% of Vol_{max}), when skin thickness = 1mm

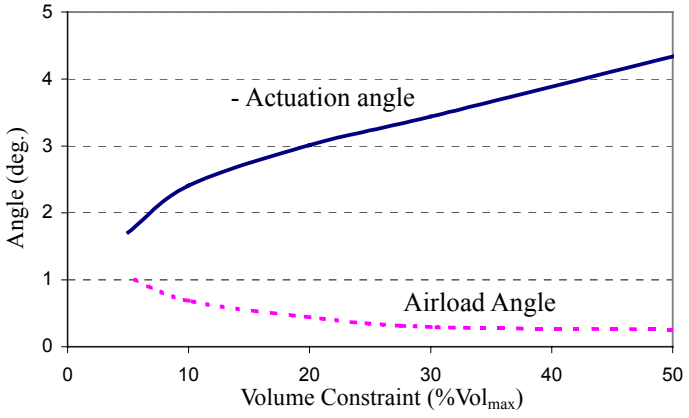

Figure 15: Variations in airload and actuation angles of the CGT optimized structures as functions volume constraint

As the volume constraint reduces, the optimized structure contains less and less actuators. For the 5 and 10% volume constraint cases, the structure requires about 10 and 20 pairs of actuators, respectively (actuators that are connected to form a continuous substructure are counted as one). In comparison, there are similar structural features in all of the topologies, for example *(i)* network of actuators almost parallel to the skin in all regions, *(ii)* segmented structural support between the parallel actuators, and *(iii)* segmented structural connections from the parallel actuators to the skin. Although the lower volume solutions are less complex, the trailing edge deflection as measured by the *EFA* also decreases from 4.3° to 1.7° as the volume constraint reduces from 50 to 5% of Vol_{max}. The axial strain level of the CGT optimized structures when deflected to their maximum levels is also shown in color in Fig 14. Relatively low strain levels are distributed somewhat uniformly in interior elements, and higher strain levels are observed in skin elements throughout regions 3 and 4. The variation of the corresponding airload angle is presented in Figure 15 as volume constraint varied. As the volume constraint decreases from 50 to 5% of Vol_{max}, the airload angle increases from 0.25° to 1° due to fewer elements and thus reduced overall stiffness. For a reasonable complexity and performance, the structure optimized with volume constraint of 10% is selected to be evaluated further. The structure contains about 20 pairs of actuators and is predicted to produce an actuation angle of 2.4° and a deformation equivalent to 0.68° under the airload.

5.4.2 Skin Thickness

The effect of the skin thickness is presented in this section. Fig. 16 shows topologies, deflections, and axial strain level of the CGT optimized structures when the thickness of the skin elements is 1, 0.8, 0.6, 0.4, and 0.2mm (optimized with volume constraint of 10% of Vol_{max}). The results illustrate that the optimal topology changes slightly with the skin thickness. For all cases, the parallel actuators have slightly different thickness distribution and are almost at the same distance from the skin. However, the locations of segmented structural supports between the parallel actuators are different in most cases. The tip deflection angle is increased from *EFA* of 2.4° to 4.1° when the skin thickness is reduced from 1mm to 0.2mm. Variations of this actuation angle as well as the airload angle as functions of skin thickness are presented graphically in Fig. 17. As the skin thickness is reduced, both actuation and airload angles increase almost linearly but the actuation angle increases at a faster rate. The increase in airload angle is from 0.7° to 1.2° *EFA*, for the reduction of skin thickness from 1mm to 0.2mm. Therefore, it is possible to increase the actuation angle to 4.1° by just reducing the skin thickness to 0.2mm, but the airfoil deflection of 1.2° under the airloads may be unacceptably high.

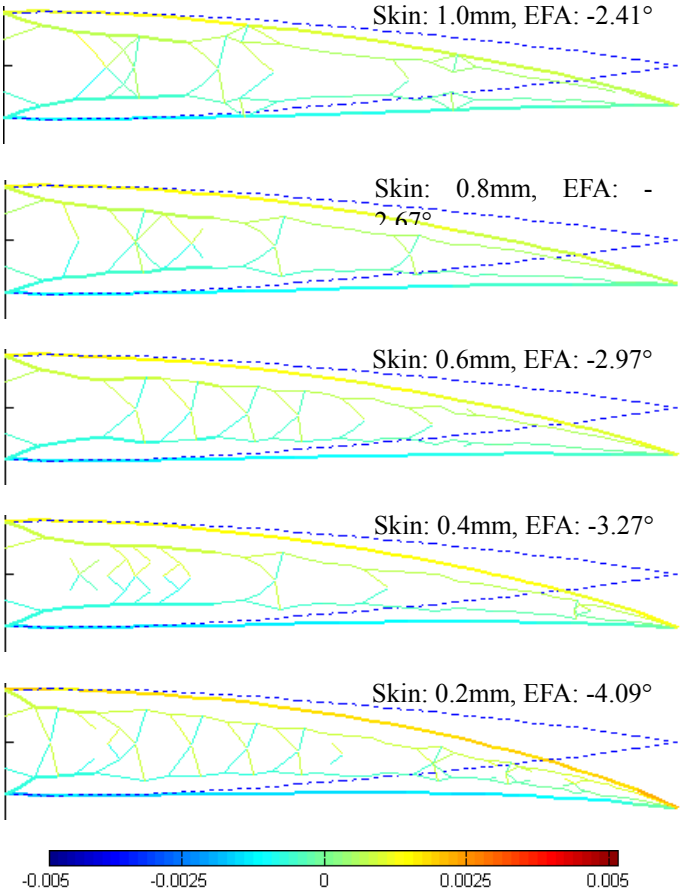

Figure 16: Topologies, deformations (7x), and axial strain level (color coded) of CGT optimized structures for different skin thickness (1, 0.8, 0.6, 0.4, and 0.2mm), when volume constraint is 10% of Vol_{max}

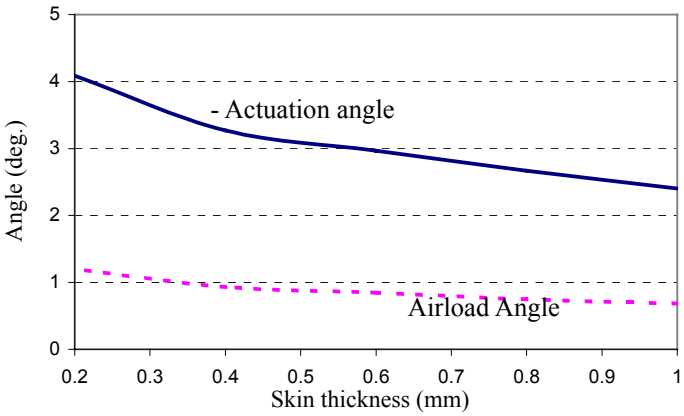

Figure 17: Variations in airload and actuation angles of the CGT optimized structures as functions skin thickness

The results in this section show that the reduction in skin thickness can effectively increase the actuation angle, but leads to reduction in overall structural stiffness of the airfoil itself, since skin thickness contributes to both skin axial and bending stiffness. For the monolithic aluminum skin, which is an isotropic material, the relationship between axial and bending stiffness of the skin is fixed. However for other types of skins such as sandwiched composite skins the relationship between axial and bending stiffness may be controlled to maximize the performance.

5.5 Preliminary Design of Skin

This section examines the effect of variations in skin axial and bending stiffness. The change in axial and bending stiffness is introduced by changing the skin cross sectional area and skin area moment of inertia, respectively. The skin inertia and area are varied independently, and are increased or reduced by multiplication factors that are varied from 0.001 to 1000. For any combination of skin stiffnesses, the substructure topology and geometry is optimized using the concurrent optimization with volume constraint of 10% of Vol_{max}. Figure 18 shows contour plot of the objective function, *J*, as a function of the skin inertia and area factors. The baseline configuration corresponds to skin inertia and area of the aluminum skin with 1mm thickness, and is shown as a circle in the middle of Figure 18.

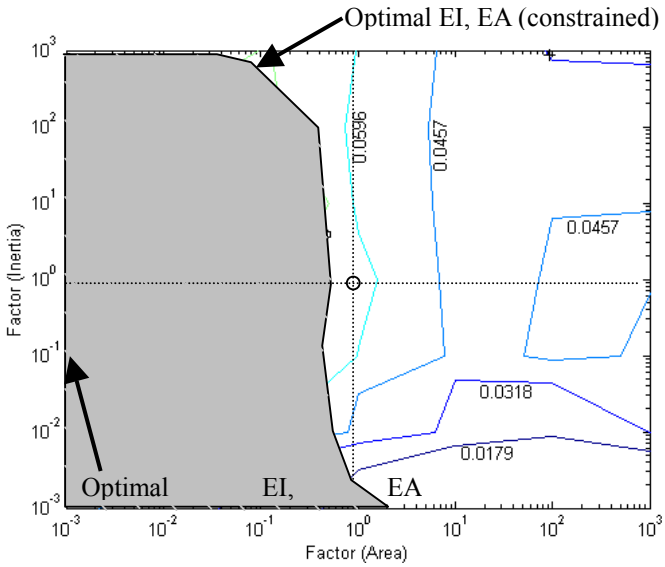

Figure 18: Contour plot of objective function, J, as function of skin parameters (shaded area represents area where airload angle is greater than 1°)

An additional constraint has been added to the plot where the shaded area indicates where the airload angle is greater than 1°. Generally, as the skin area or axial stiffness reduces, the objective function increases. The effect of the skin inertia or bending stiffness is more complex, and is highly dependent on skin axial stiffness. When the skin axial stiffness is around the

baseline value, increasing the skin inertia from the baseline produces almost no change in the objective function, but reducing the skin inertia reduces the objective function. A similar observation also holds in high skin axial stiffness regions. For the low axial stiffness region, there exists optimal skin inertia or bending stiffness (area factor of 0.001 and inertia factor of 0.1) that produces maximum objective function of 0.129, but this optimal point is well beyond constraint boundary (lying in a region that produces unacceptably high airload angles). This optimal set is referred further as optimal skin parameters for the unconstrained case. The maximum value of the objective function that satisfies the constraint is around 0.0735, which is observed when the area factor is 0.1 and the inertia factor is 500, producing a design that is not excessively compliant under aerodynamic loading. These skin parameters are optimal for the constrained case. Physically, this means that the optimal skin should have slightly lower axial stiffness and much higher bending stiffness than the original skin.

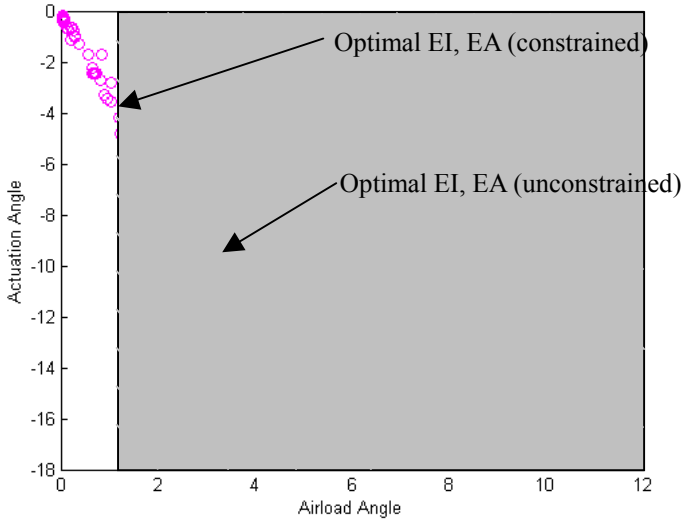

Figure 19: Performance plot for various combinations of skin parameters

For the same set of results, the performance plot of the corresponding actuation and airload angles are shown in Fig. 19. For most cases the ratio between the airload and actuation angles are almost constant as depicted by the nearly linear relationship between the angles. The actuation and airload angles that correspond to the optimal skin parameters are 10.62° and 3.58° (without the constraint) and 3.7° and 1° (with the constraint). The optimal skin parameters are defined previously as a set of area and inertia factors that produces maximum objective function. Contour plots of actuation angle as functions of the skin inertia and area factors are presented in Fig. 20. Again, the actuation angle is increased as the skin area or axial stiffness decreases, and the effect of the skin inertia or bending stiffness differs depending on the value of the skin axial stiffness. When the axial stiffness is close to the baseline value or higher, decreasing the skin inertia produces slight increases in the actuation and airload angles. In the low axial stiffness region, reduction the skin inertia also leads to increases in both of the angles but the increases are much more than that in higher axial stiffness regions.

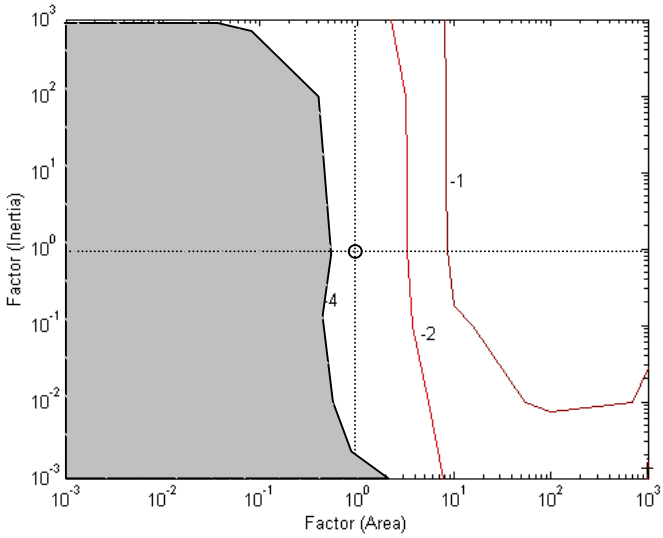

Figure 20: Contour plot of actuation angle as function of skin parameters (shaded area represents area where airload angle is greater than 1°)

6. CONCLUSIONS

Several optimization strategies for a conformable rotor airfoil using distributed piezoelectric actuators are developed and evaluated. The design optimization techniques determine optimal actuator distributions that simultaneously produce significant trailing edge deflection under actuation loads, but minimize airfoil deflection under aerodynamic loads. This is achieved by optimizing a multi-criteria objective function that contains a ratio of energy functions: Mutual Potential Energy, and Strain Energy, representing the deflections due to the actuation and aerodynamic loads, respectively. Actuator topology and geometry are optimized using concurrent geometry-topology optimizations. The optimal structure is systematically simplified using the optimization process and reducing the allowable active material to obtain a design that is less complex and satisfies all the requirements. Some of the key observations of the present study are presented next.

For a relaxed volume constraint design (more active material), the airfoil structure optimized using the geometry optimization is predicted to generate 3.42° *EFA* under the actuation loads, and the airfoil deformed by only 0.25° under the aerodynamic loads. In the geometry optimization, the active elements near the spar were moved toward the skin, and after mid chord the active elements began the transition by gradual shifting away from the skin.

The optimized airfoil section using Concurrent Geometry-Topology (CGT) optimization is predicted to produce an *EFA* of 4.3° under the actuation loads. Key features of this structure were similar to that of the geometry optimized airfoil except that the CGT optimized structure had did not have a distinct transition area where the active elements gradually shifting. The strain distribution was relatively uniform in interior elements, and higher strain levels were observed in the skin elements from mid chord to the trailing edge.

By reducing the volume constraint and skin thickness a simpler (and possibly easier to fabricate) design was obtained and evaluated. Optimal values for the skin axial and bending stiffness were obtained in a parametric optimization, and this optimal conformable airfoil is predicted to produce *EFA* of 3.7° under actuation loads and less than 1° under aerodynamic loads. The optimal skin should have less axial stiffness and much more bending stiffness as compared to the 1mm aluminum skin used as the baseline design.

ACKNOWLEDGEMENT

The authors gratefully acknowledge the support of the National Rotorcraft Technology Center through the Penn State Rotorcraft Center, with Dr. Yung Yu serving as the technical monitor.

REFERENCES

[1] Milgram, J., Chopra, I. and Straub, F., 1998, "Rotors with Trailing Edge Flaps: Analysis and Comparison with Experimental Data," *Journal of the American Helicopter Society*, **43**(4), pp. 319-332.

[2] Bernhard, A. P. F. and Chopra, I., 1998, "Hover Testing of Active Rotor Blade-Tips Using a Piezo-Induced Bending-Torsion Coupled Beam," *Journal of Intelligent Material Systems and Structures*, **9**(12), pp. 963-974.

[3] Myrtle, T. and Friedmann, P., 2001, "Application of a New Compressible Time Domain Aerodynamic Model to Vibration Reduction in Helicopters Using an Actively Controlled Flap," *Journal of the American Helicopter Society*, **46**(1), pp. 32-43.

[4] Straub, F., and King, R., 1996, "Application of Smart Materials to Control of a Helicopter Rotor*," Proc. SPIE's Symposium on Smart Structures and Materials*, San Diego.

[5] Lee, T. and Chopra, I., 2000, "Design Issues of a High-Stroke, On-Blade Piezostack Actuator for a Helicopter Rotor with Trailing-Edge Flaps," *Journal of Intelligent Material Systems and Structures*, **11** (5), pp. 328-342.

[6] Clement, J. W., Brei, D, and Barret, R., 1999, "Wind Tunnel Testing of a High Authority Airspeed Insensitive Rotor Blade Flap" *Proc. 40th AIAA/ASME/ASCE/AHS/ASC Structures, Structural Dynamics, and Materials Conference and Exhibit*, St. Louis, MO, pp 2414-2424.

[7] Chattopadhyay, A., Seeley, C. E., and Mitchell, L., 1997, "Design of A Smart Flap Using Polymeric C-Block Actuators and A Hybrid Optimization Technique," *Smart Materials and Structures*, **6**(2), pp. 134-144.

[8] Hall, S., Tzianetopolou, T., Straub, F., and Ngo, H., 2000, "Design and Testing of a Double X-Frame Piezoelectric Actuator," Proc. *SPIE Conference on Smart Structures and Materials*, New Port Beach, CA.

[9] Straub, F., Ngo, H. T., Anand, V. and Domzalski, D., 2001, "Development of a Piezoelectric Actuator for Trailing Edge Flap Control of Full Scale Rotor Blades," *Smart Materials and Structures*, **10** (1), IOP, Bristol, England, pp. 25-34.

[10] Koratkar, N.A. and Chopra, I., 2002, "Wind Tunnel Testing of a Smart Rotor Model With Trailing-Edge Flaps," *Journal of the American Helicopter Society*, **47**(4), pp. 263-272.

[11] Fulton, M. and Ormiston, R.A., 2001, "Hover Testing of a Small-Scale Rotor with on-blade Elevons," *Journal of the American Helicopter Society*, **46**(2), pp. 96-106.

[12] Ormiston, R., 1991, "Can Smart Materials Make Helicopters Better," 4th ARO Workshop on Dynamics and Aeroelastic Stability Modeling of Rotorcraft Systems, College Park, MD.

[13] Saggere, L. and Kota, S., 1999, "Static Shape Control of Smart Structures using Compliant Mechanisms," *AIAA Journal*, **37** (5).

[14] Lagoudas, D. and Strelec, J., 2000, "Intelligent Design Optimization of a Shape Memory Alloy Actuated Reconfigurable Wing," *Proc. SPIE Conference on Smart Structures and Materials*, New Port Beach, CA, pp. 338-348.

[15] Bein, Th., Hanselka, H and Breitbach, E. 2000 "Adaptive Spoiler to Control the Transonic Shock," *Smart Materials and Structures*, **9** (2), IOP, Bristol, England, pp 141-148

[16] Kudva, J, Sanders, B., Pinkerton-Florance, J., and Garcia, E., 2001, "Overview of DARPA/AFRL/NASA Smart Wing Phase 2 Program," *Proc. SPIE Conference on Smart Structures and Materials*, New Port Beach, CA, pp. 383-389.

[17] Raney, D., Montgomery, R., Green, L and Park, M., 2000, "Flight Control Using Distributed Shape-Change Effector Arrays," *Proc. 41st AIAA/ASME/ASCE/AHS/ASC Structures, Structural Dynamics, and Materials Conference and Exhibit*, Atlanta, GA, pp. 156-167.

[18] Ananthasuresh, G. and Kota, S., 1995, "Designing Compliant Mechanisms," *Mechanical Engineering*, pp. 93-96.

[19] Ananthasuresh, G.K., 2001, "Manufacturing Issues in Integrated Systems of Small Size," *Journal of Materials Processing & Manufacturing Science*, **8**, pp. 327-329

[20] Frecker, M., Ananthasuresh, G.K., Nishiwaki, S., Kikuchi, N. and Kota, S., 1997, "Topological Synthesis of Compliant Mechanisms Using Multi-Criteria Optimization," *ASME Journal of Mechanical Design*, **119**(2), pp. 238-245.

[21] Frecker, M. and Canfield, S., 2000, "Optimal Design and Experimental Validation of Compliant Mechanical Amplifiers for Piezoceramic Stack Actuators," *Journal of Intelligent Material Systems and Structures*, **2** (5), pp. 360-369

[22] Yin, L. and Ananthasuresh, G., 2001, "Topology Optimization of Compliant Mechanisms with Multiple Materials Using a Peak Function Material Interpolation Scheme," *Structural and Multidisciplinary Optimization*, **23** (1), pp. 49-62.

[23] Kota, S., Hetrick, Z. Li and Saggere, L., 1999, "Tailoring Unconventional Actuators Using Compliant Transmissions: Design Methods and Applications," *IEEE/ASME Transactions on Mechatronics*, **4**(4), pp. 396-408.

[24] Sigmund, O., 2001, "Design of Multiphysics Actuators Using Topology Optimization - Part II: Two-Material Structures," *Computer Methods in Applied Mechanics and Engineering*, **190** (5), pp. 6605-6627.

[25] Silva, E. C. N., Nishiwaki, S., and Kikuchi, N., 2000, "Topology Optimization design of Flextensional Actuators," *IEEE Transactions on Ultrasonics, Ferroelectrics, and Frequency Control,* **47**(3), pp. 657-671.

[26] Abbot, I.H. and Von Doenhoff, A.E., 1959, *Theory of Wing Sections*, Dover, New York.

[27] Katz, J. and Plotkin, A., 1991, *Low-Speed Aerodynamics: From Wing Theory to Panel Methods*, McGraw-Hill Inc., New York.

[28] Shield, R.T. and Prager, W., 1970, "Optimal Structural Design for Given Deflection," *Journal of Applied Mathematics and Physics*, **21**(7), pp. 513-523.

[29] Sarjeant, R. A., Frecker, M., and Gandhi, F. S., 2002, "Optimal Design of A Smart Conformable Rotor Airfoil," Proceedings of the Adaptive Structures and Material Systems Symposium, International Mechanical Engineering Congress and Exposition (Winter Meeting of the ASME), New Orleans, LA.

APPENDIX

Sensitivity Analysis for Geometry Optimization

The gradient of the objective function (Eq. 10) with respect to geometry variables, Δx_j and Δy_j, can be calculated. This section only provides the derivation of the gradient with respect to Δx_j since an identical method can be applied to obtain the gradient with respect to Δy_j. The derivative of the objective function with respect to Δx_j is given by Eq. A1.

$$\frac{\partial J}{\partial \Delta x_j} = \frac{SE\,\frac{\partial MPE}{\partial \Delta x_j} - MPE\,\frac{\partial SE}{\partial \Delta x_j}}{SE^2} \tag{A1}$$

$$\frac{\partial MPE}{\partial \Delta x_j} = \frac{\partial v^T}{\partial \Delta x_j} Ku + v^T \frac{\partial K}{\partial \Delta x_j} u + v^T K \frac{\partial u}{\partial \Delta x_j}$$

$$\frac{\partial SE}{\partial \Delta x_j} = w^T \frac{\partial K}{\partial \Delta x_j} w + 2 w^T K \frac{\partial w}{\partial \Delta x_j}$$

The derivatives of the displacement fields, and structural stiffness (with respect to Δx_j) are required, and they can be calculated using Eq. A2.

$$\frac{\partial u}{\partial \Delta x_j} = K^{-1}\left(\frac{\partial F_{act}}{\partial \Delta x_j} - \frac{\partial K}{\partial \Delta x_j} u\right) \tag{A2}$$

$$\frac{\partial v}{\partial \Delta x_j} = K^{-1}\left(\frac{\partial F_{dummy}}{\partial \Delta x_j} - \frac{\partial K}{\partial \Delta x_j} v\right)$$

$$\frac{\partial w}{\partial \Delta x_j} = K^{-1}\left(\frac{\partial F_{aero}}{\partial \Delta x_j} - \frac{\partial K}{\partial \Delta x_j} w\right)$$

$$\frac{\partial K}{\partial \Delta x_j} = \sum_k \frac{\partial k_k}{\partial \Delta x_j}$$

where k_k is the elemental stiffness matrix of the active elements that connect to the j[th] node. The derivatives of the active, aerodynamic, and dummy forces seen in Eq. A2 are defined as follows:

$$\frac{\partial F_{act}}{\partial \Delta x_j} = \sum_k \frac{\partial f_{act}^k}{\partial \Delta x_j} \tag{A3}$$

$$\frac{\partial F_{dummy}}{\partial \Delta x_j} = 0$$

$$\frac{\partial F_{aero}}{\partial \Delta x_j} = 0$$

where f_{act}^k is the elemental load vector of the active elements that attach to the j[th] node. By substituting Eqs. A3 and A2 into Eq. A1, the derivatives of the MPE and SE with respect to Δx_j are summarized in Eq. A4.

$$\frac{\partial MPE}{\partial \Delta x_j} = v^T \frac{\partial F_{act}}{\partial \Delta x_j} - v^T \frac{\partial K}{\partial \Delta x_j} u \tag{A4}$$

$$\frac{\partial SE}{\partial \Delta x_j} = -w^T \frac{\partial K}{\partial \Delta x_j} w$$

It should be noted that detail derivations of $\frac{\partial F_{act}}{\partial \Delta x_j}$ and $\frac{\partial K}{\partial \Delta x_j}$ are not provided here.